

Reaction dynamics of $\text{OH}^+(\text{}^3\Sigma^-) + \text{C}_2\text{H}_2$ studied with crossed beams and density functional theory calculations

Li Liu, Courtney Martin, and James M. Farrar^{a)}*Department of Chemistry, University of Rochester, Rochester, New York 14627*

(Received 26 April 2006; accepted 17 May 2006; published online 4 October 2006)

The reactions between $\text{OH}^+(\text{}^3\Sigma^-)$ and C_2H_2 have been studied using crossed ion and molecular beams and density functional theory calculations. Both charge transfer and proton transfer channels are observed. Products formed by carbon-carbon bond cleavage analogous to those formed in the isoelectronic $\text{O}(\text{}^3P) + \text{C}_2\text{H}_2$ reaction, e.g., ${}^3\text{CH}_2 + \text{HCO}^+$, are not observed. The center of mass flux distributions of both product ions at three different energies are highly asymmetric, with maxima close to the velocity and direction of the precursor acetylene beam, characteristic of direct reactions. The internal energy distributions of the charge transfer products are independent of collision energy and are peaked at the reaction exothermicity, inconsistent with either the existence of favorable Franck-Condon factors or energy resonance. In proton transfer, almost the entire reaction exothermicity is transformed into product internal excitation, consistent with mixed energy release in which the proton is transferred with both the breaking and forming bonds extended. Most of the incremental translational energy in the two higher-energy experiments appears in product translational energy, providing an example of induced repulsive energy release. © 2006 American Institute of Physics. [DOI: 10.1063/1.2212417]

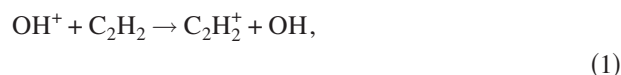
I. INTRODUCTION

The reactions of triplet state oxygen atoms with the unsaturated hydrocarbons ethylene and acetylene provide a number of interesting comparisons and contrasts.¹ In the ethylene case, the initially formed oxirane diradical generated by C–O bond formation first undergoes rapid intersystem crossing, following which either hydrogen atom emission to form the vinyloxy radical or C–C bond cleavage to form $\text{CH}_3 + \text{HCO}$ occurs. In contrast, the reaction with acetylene, which also involves incipient C–O bond formation and competition between H-atom emission or C–C bond cleavage, appears to take place entirely on the triplet surface.

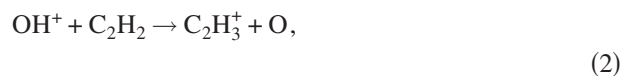
In a recent study from our laboratory, we presented a detailed experimental and theoretical study of the charge transfer and hydride transfer reactions that occur between the hydroxyl cation in its ground ${}^3\Sigma^-$ electronic state and ethylene.² Like the isoelectronic neutral $\text{O}(\text{}^3P) + \text{C}_2\text{H}_4$ system, reactive processes are initiated by C–O bond formation, yielding a protonated oxirane triplet diradical, which undergoes intersystem crossing to the singlet manifold. On the singlet surface, the diradical undergoes ring closure to form an epoxide, and following a hydrogen atom migration, reopens and cleaves the nascent C–O bond to yield the vinyl cation and H_2O . Although rapid intersystem crossing appears to be operative both in the ionic and the neutral case, in the latter, the nascent C–O bond survives and the vinyloxy radical decays by H-atom emission or by C–C bond cleavage. In the ionic system, in contrast, the nascent C–O bond cleaves to form $\text{C}_2\text{H}_3^+ + \text{H}_2\text{O}$ products. In addition to this process,

which is accessed by small impact parameters, charge transfer to yield $\text{C}_2\text{H}_4^+ + \text{OH}$ occurs in a facile manner.

As part of a series of investigations from this laboratory on reactions of oxygen-containing ions with unsaturated hydrocarbons,^{3–5} we present a study of the $\text{OH}^+ + \text{C}_2\text{H}_2$ system in order to elucidate the role of intersystem crossing and to explore analogies with the reactive pathways in the isoelectronic neutral $\text{O}(\text{}^3P) + \text{C}_2\text{H}_2$ system. We are not aware of any previous studies on the $\text{OH}^+ + \text{C}_2\text{H}_2$ system. The isoelectronic system $\text{O}(\text{}^3P) + \text{C}_2\text{H}_2$ has been investigated by a number of groups;⁶ molecular beam experiments have been particularly insightful in demonstrating that a triplet state diradical transient complex is formed, and that product formation is governed by its decay via C–C bond cleavage to form triplet methylene and carbon monoxide as well as hydrogen atom emission leading to the ketylenyl radical HCCO. On the basis of the proton affinity of CO, one might expect to see ${}^3\text{CH}_2 + \text{HCO}^+$ products for the title reaction with an exothermicity of 309 kJ/mol. However, we did not observe this reaction channel in the experiments; only charge transfer and proton transfer channels were observed:



$$\Delta H = -156 \text{ kJ/mol } (-1.62 \text{ eV}),$$



$$\Delta H = -173 \text{ kJ/mol } (-1.79 \text{ eV}).$$

The absence of products formed by carbon-carbon bond cleavage suggests that in analogy with the ethylene system, the specific decay paths of transient intermediates must be examined. This paper describes the investigation of the

^{a)}Author to whom correspondence should be addressed. Electronic mail: farrar@chem.rochester.edu

$\text{OH}^+ + \text{C}_2\text{H}_2$ reaction using crossed ion and molecular beams. In conjunction with computations of the structures of important reactive intermediates and their isomerization rates, our study provides additional information on the reactive pathways and dynamics both experimentally and theoretically.

II. EXPERIMENTAL METHOD

The experimental apparatus has been described previously,⁷ so only a brief review is made here. Ground electronic state OH^+ ions were produced by electron impact on water vapor. The measured pressure in the initial focusing stage vacuum chamber was about 4.5×10^{-5} Torr. The pressure in the ion source was typically 10^{-2} Torr. The internal energy distribution of the ions was not characterized, but product energy partitioning described below was consistent with reactants that had only small amounts of internal excitation. The reactant ions were accelerated to 300 V, and the desired ions were then mass selected with a 60° magnetic sector. After deceleration to the desired beam energy and focusing by a series of ion optics, the beam had an energy distribution with a full width at half maximum (FWHM) of 0.25–0.35 eV in these experiments. Experiments were performed at selected energies over a relative collision energy range of 0.39–1.18 eV. The acetylene gas (98%) was first passed through a cold trap to remove the acetone impurity. The neutral beam was formed by supersonic expansion of the pure gas through a 0.07 mm nozzle. In the main chamber, the neutral beam intersected the ion beam at 90° . A tuning fork chopper modulated the neutral beam at 30 Hz, allowing the separation of background from the true reactive scattering signal. An electrostatic energy analyzer with a resolution of 0.07 eV was used to measure the kinetic energy distributions of the reactant and product ions. The energy analyzer was calibrated before and after the experiments. The resonant charge transfer reaction between He^+ and He was used to determine the zero offset of the energy analyzer. The product ions were mass analyzed by a quadrupole mass spectrometer and detected by a dual microchannel plate ion detector.

Two independent measurements were performed in each experiment. The kinetic energy distributions of the scattered product ions were measured at 17–23 fixed laboratory angles based on the signal levels. These kinetic energy distributions were then normalized by measuring angular distributions of product ions in the laboratory coordinate system by summing up the signal over all energies. The angular distributions were corrected for beam drifting and detection efficiency by returning to a reference angle periodically and assuming that the drift of the signal is linear in time. These measurements were carried out for every selected laboratory energy.

III. DATA ANALYSIS

Dynamical interpretation of the experimental data is facilitated by transformation of the measured kinetic energy and angular distributions of products to the center of mass (c.m.) coordinates. The reactant beams in the experiments have velocity and angular spreads, resulting in distributions of collision energies and intersection angles. The laboratory flux at a particular scattering angle and velocity is expressed

as an integral of the c.m. cross section over the beam velocity distributions $f_i(v_i)$, summed over final quantum states n according to Eq. (3):

$$I_{\text{lab}}(v, \Theta) = v^2 \int_0^\infty dv_2 f_2(v_2) \int_0^\infty dv_1 f_1(v_1) \frac{V_{\text{rel}}}{u^2} \times \sum_n I_{\text{c.m.}}(u_n, \theta; V_{\text{rel}}) \delta(u - u_n). \quad (3)$$

An iterative deconvolution procedure is used to extract the c.m. cross section from the laboratory flux distributions by inverting the following equation:⁸

$$I_{\text{lab}}(v, \Theta) = \sum_{i=1}^N f_i \frac{v^2}{u_i} I_{\text{c.m.}}(u_i, \theta_i). \quad (4)$$

In this expression, v and u_i are the velocities in the laboratory and c.m. coordinates, respectively. The functions denoted f_i are the weighing factors for Newton diagram i based on the reagent beam distributions. The extracted $I_{\text{c.m.}}(u, \theta)$ can be transformed back to the laboratory frame, allowing comparison between the results of the deconvolution and the experimental data. Five points are used to represent the energy distributions of each of the two reagent beams, and five points represent the intersection angle distribution; thus, in the above equation, N is 125.

The barycentric angular distribution $g(\theta)$ of the products can be calculated by integrating the derived $I_{\text{c.m.}}(u, \theta)$ over product speed.⁹ The function $g(\theta)$ represents the relative intensities of products scattered into c.m. scattering angle θ averaged over product kinetic energy, evaluated by integration over c.m. speed u , as follows:

$$g(\theta) = \int_0^\infty I_{\text{c.m.}}(u, \theta) du. \quad (5)$$

Similarly, the angle-averaged relative translational energy distributions of products, $P(E_T')$, are calculated by integrating the c.m. intensity over the appropriate angular range as indicated by

$$P(E_T') = \int_0^\pi u^{-1} I_{\text{c.m.}}(u, \theta) \sin \theta d\theta. \quad (6)$$

The full flux distributions in velocity space as well as the kinetic energy and angular distributions derived from them provide important physical insight into the nature of reactive collisions.

IV. RESULTS

The charge transfer reaction $\text{OH}^+ + \text{C}_2\text{H}_2 \rightarrow \text{C}_2\text{H}_2^+ + \text{OH}$ was studied at collision energies of 0.39, 0.75, and 1.15 eV. This threefold range of collision energies extends to the lower limit of our instrumentation, probing attractive features of the potential energy surface, but is also large enough to observe the onset of repulsive energy release brought about by the accessibility of short range portions of the potential energy surface. Figure 1 shows the center of mass flux distribution of the C_2H_2^+ products at the lowest collision energy of 0.39 eV, obtained by iterative deconvolution as de-

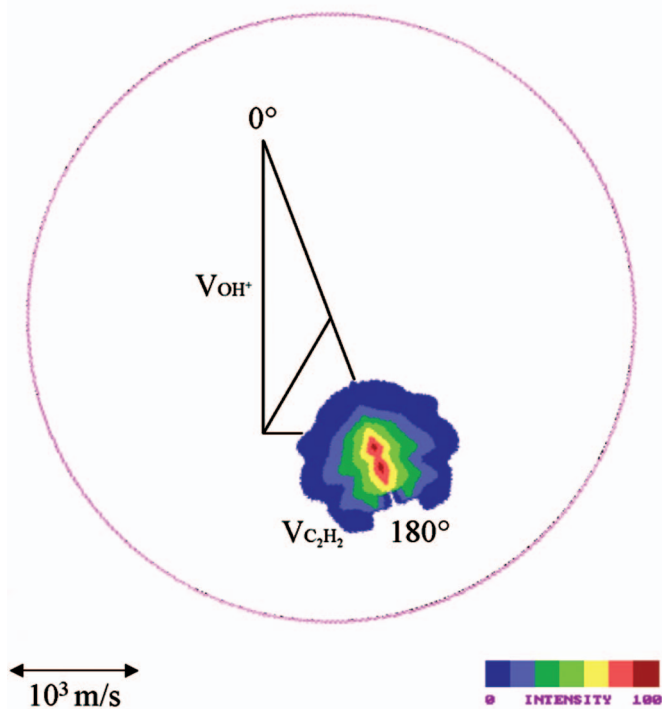
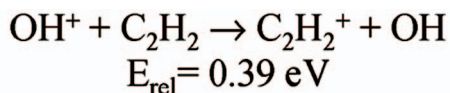


FIG. 1. (Color) Newton diagram and scattered C_2H_2^+ product flux contour map at the collision energy of 0.39 eV.

scribed previously. The distributions at two higher energies are qualitatively similar. In the c.m. coordinate system, the directions of the OH^+ ion beam and C_2H_2 neutral beam are 0° and 180° , respectively.

The experimental results shown in the flux map indicate that the charge transfer flux distribution is sharply asymmetric. The majority of the C_2H_2^+ products are scattered in the same direction as the precursor C_2H_2 beam, and with similar velocities. These forward-scattered products indicate that the charge transfer reaction is dominated by a direct mechanism, proceeding through large impact parameter collisions on a time scale much shorter than a rotational period of the transient association complex of the approaching reactants.

The angular distributions and relative translational energy distributions of the charge transfer products at all three energies are shown in Fig. 2. The widths of the angular distributions show a slight narrowing with increasing collision energy, consistent with decreased interaction times at higher kinetic energies. As the collision energy increases, the relative translational energy distributions of the products shift towards higher energies and increase in width.

The energy partitioning results are summarized in Table I. The total energy is the sum of collision energy, any reactant internal energy (set equal to zero here), and the reaction exothermicity. The supersonic expansion produces internally cold neutral reactants. The product relative energy E_T' at each collision energy is tabulated as the average value of the appropriate relative translational energy distribution in Fig. 2(b). From energy conservation, we determine that the frac-

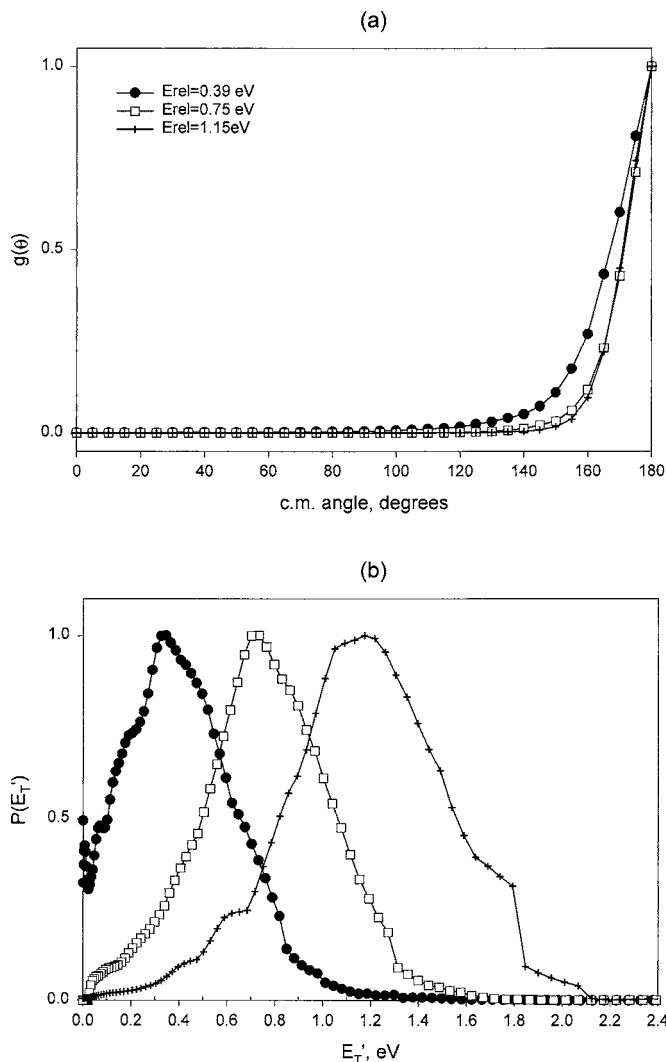


FIG. 2. (a) Angular distributions and (b) relative translational energy distributions for C_2H_2^+ products in c.m. coordinates at all energies.

tion of the total energy appearing in product translation increases from 21% to 43% as the collision energy spans the full range studied here. The average internal energy of the reaction products ranges from 1.58 to 1.60 eV at all collision energies, identical to the reaction exothermicity of 1.62 eV within 3%. Therefore, the internal energy distributions of the charge transfer products are essentially independent of collision energy in the range of these experiments.

The proton transfer reaction $\text{OH}^+ + \text{C}_2\text{H}_2 \rightarrow \text{C}_2\text{H}_3^+ + \text{O}$ was studied at 0.39, 0.71, 1.18 eV. Figure 3 shows the flux distribution for the C_2H_3^+ products at the lowest collision

TABLE I. Energy results at different relative energies (in eV) for $\text{OH}^+ + \text{C}_2\text{H}_2 \rightarrow \text{OH} + \text{C}_2\text{H}_2^+$.

Ion energy	0.575	1.170	1.839
Reactant relative energy, E_{rel}	0.389	0.748	1.153
Total energy, E_{total}	2.006	2.365	2.770
Product average relative energy, $\langle E_T' \rangle$	0.425	0.768	1.186
$\langle E_T' \rangle / E_{\text{total}}$ (%)	21.20	32.50	42.80
Product average internal energy	1.581	1.597	1.584
$Q = \langle E_T' \rangle - E_{\text{rel}}$	0.036	0.020	0.033

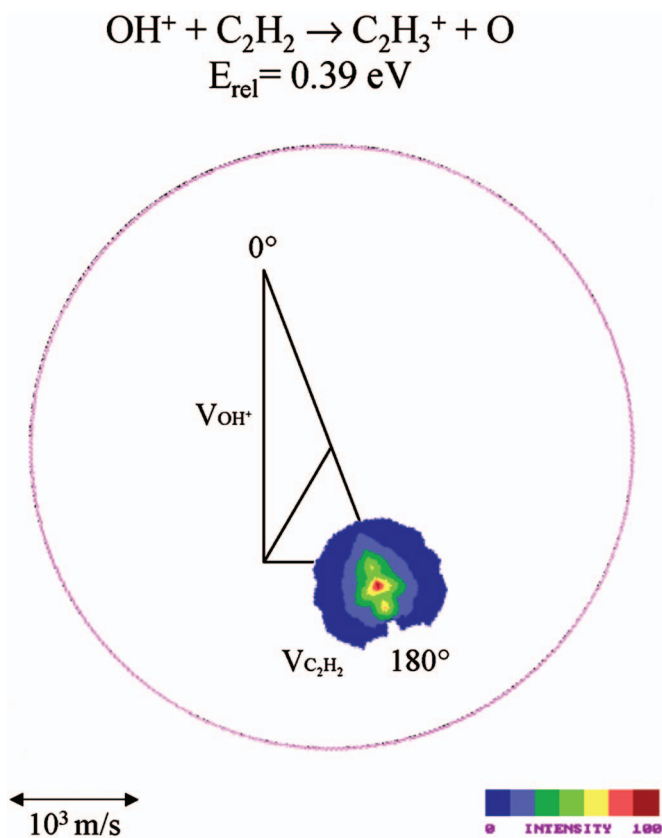


FIG. 3. (Color) Newton diagram and scattered C_2H_3^+ product flux contour map at the collision energy of 0.39 eV.

energy of 0.39 eV. The major feature of this distribution is both qualitatively and quantitatively similar to that shown in Fig. 1 for the charge transfer reaction, showing strong asymmetry, with a maximum near the precursor acetylene reactant velocity. The distributions at the two higher collision energies are similar to that shown in Fig. 3. This strongly direct mechanism is characteristic of an exothermic proton transfer reaction.

For each energy, the product angular distribution and relative translational energy distribution are shown in Fig. 4, with numerical results summarized in Table II. The translational energy distributions are very similar to those of charge transfer products in that they broaden and shift with increasing collision energy. The results in the energy table show that the average internal energies of reaction products increase slightly as collision energy increased.

V. COMPUTATIONAL STUDIES

The experimental data for the $\text{OH}^+ + \text{C}_2\text{H}_2$ system show clearly that the exclusive reactive processes are proton and charge transfer, occurring through large impact parameter collisions. These results contrast with the isoelectronic $\text{O}(^3P) + \text{C}_2\text{H}_2$ system, in which reactions involving formation and cleavage of bonds among the heavy atoms dominate the reaction dynamics. The neutral system has been studied in crossed molecular beams by Schmoltnner *et al.*,¹⁰ Clemo *et al.*,¹¹ and Capozza *et al.*¹² The first of those studies found that the reactive processes to form $\text{CH}_2 + \text{CO}$ and $\text{HCCO} + \text{H}$ appear to proceed on the initially accessed triplet sur-

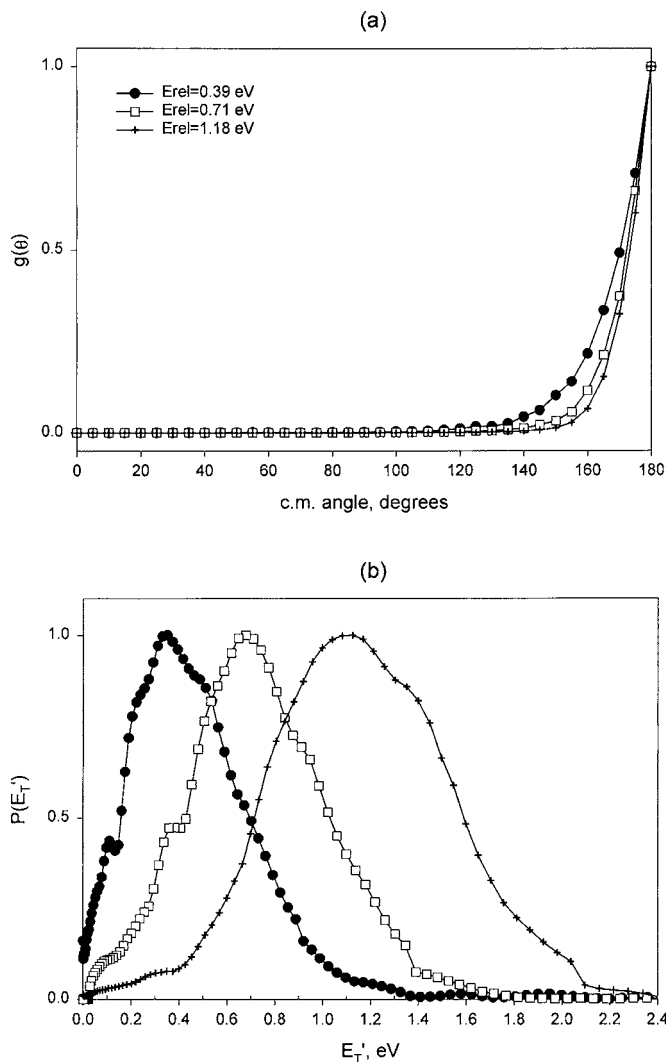


FIG. 4. (a) Angular distributions and (b) relative translational energy distributions for C_2H_3^+ products in c.m. coordinates at all energies.

face, in contrast with the related system $\text{O}(^3P) + \text{C}_2\text{H}_4$, in which facile intersystem crossing of the initially formed triplet diradical to the ground state occurs. Studies from this laboratory on the $\text{OD}^+ + \text{C}_2\text{H}_4$ system² also show that intersystem crossing to the singlet surface controls the dynamics of C_2H_3^+ formation. The distinction between the reactivities of C_2H_2 and C_2H_4 with $\text{O}(^3P)$ and $\text{OH}^+(^3\Sigma^-)$ may originate from the relative energies of the triplet and singlet states of the intermediates and the spin-orbit couplings that arise from the favorable orientations of the orbitals containing unpaired electrons.¹³ *Ab initio* calculations indicate that intersystem

TABLE II. Energy results at different relative energies (in eV) for $\text{OH}^+ + \text{C}_2\text{H}_2 \rightarrow \text{O} + \text{C}_2\text{H}_3^+$.

Ion energy	0.571	1.166	1.886
Reactant relative energy, E_{rel}	0.386	0.713	1.181
Total energy, E_{total}	2.174	2.501	2.969
Product average relative energy, $\langle E_T' \rangle$	0.520	0.747	1.173
$\langle E_T' \rangle / E_{\text{total}}$ (%)	23.90	29.90	39.50
Product average internal energy	1.654	1.754	1.796
$Q = \langle E_T' \rangle - E_{\text{rel}}$	0.134	0.034	-0.008

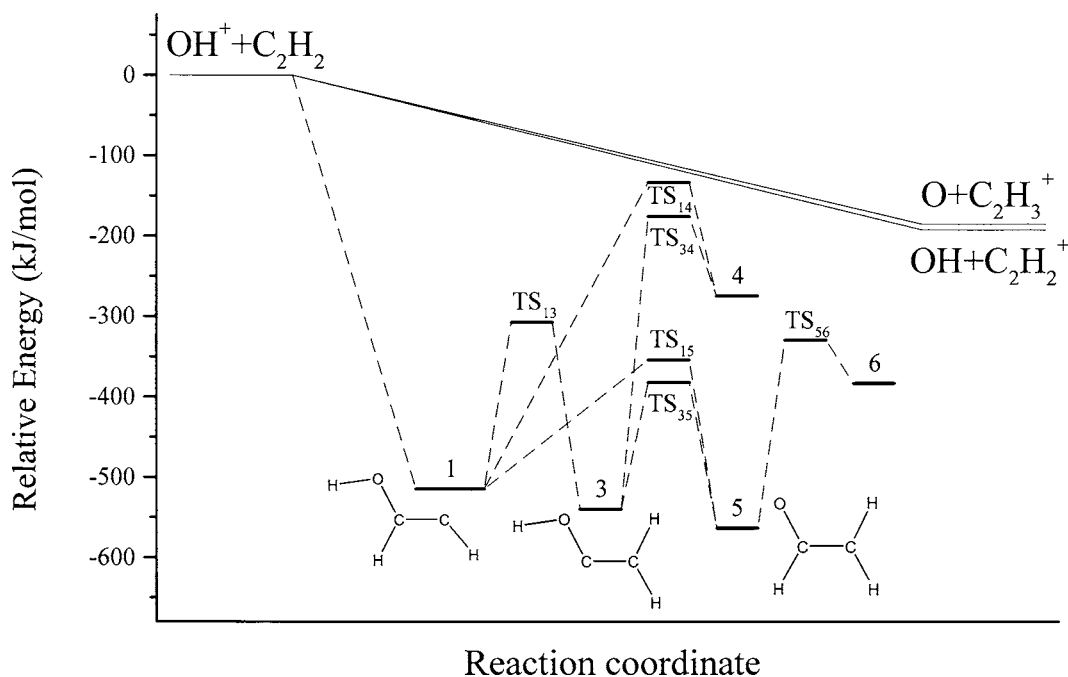


FIG. 5. Schematic reaction coordinate for the $\text{OH}^+ + \text{C}_2\text{H}_2$ reaction.

crossing is important in the ethylene-based system;¹⁴ however, calculations on the acetylene-based system¹⁵ suggest that reaction occurs on the triplet surface.

In order to understand the role that possible reactive intermediates and the transition states connecting them play in the present system, we performed density functional theory calculations with the GAUSSIAN 98 program package.¹⁶ The calculations focused on the structures of intermediates with triplet multiplicity. The geometries of all the relevant species were fully optimized at the B3LYP/6-311+G* level of theory and their vibrational frequencies were then extracted in the harmonic approximation. Single point energy calculations were performed at the same level of theory based on the geometries and zero-point vibrational energies. Figure 5 shows the reaction coordinate diagram including the energies of key reactive intermediates and transition states. A complete tabulation of the computational results with sketches of all intermediates is summarized in Ref. 17.

The protonated acetylene product, C_2H_3^+ , has two stable isomers. The classical structure of C_2H_3^+ with two hydrogen atoms bound to one carbon atom lies about 5 kJ/mol below the nonclassical structure in which one hydrogen atom bridges the two carbon atoms. This result is in agreement with the work of Lee and Schaefer.¹⁸

The density functional theory (DFT) calculations show that reactants approaching on the lowest triplet state surface generate two different initial intermediates, depending on the details of the approach geometry. The first intermediate, a triplet diradical cation, is characterized by incipient C–O bond formation, denoted on Fig. 5 by structure 1. The bond order of the C–C bond is 1.75, confirming that this structure corresponds to an enol isomer of the $[\text{C}_2\text{H}_3\text{O}]^+$ system. Four different isomers of this structure are possible, depending on the relative orientations of the hydrogen atoms bound to oxygen and to the vicinal carbon atom. All of these isomers lie

approximately 500–515 kJ mol⁻¹ below the reactants. A second intermediate that lies ~300 kJ mol⁻¹ above structure 1, in which the oxygen end of OH^+ approaches the π cloud of acetylene along the perpendicular bisector of the C–C bond, is a three-membered ring system that isomerizes quickly to the ring-opened structure 1. For clarity, this structure is not shown in Fig. 5. The structures of all possible intermediates of nominal structure 1, and the structure of the cyclic intermediate, denoted 2, are reported in the EPAPS supplement to this paper.¹⁷

Complex 1 may undergo 1,2-hydrogen atom migration over a ~200 kJ mol⁻¹ barrier on the triplet surface to form complex 3, protonated ketene. The protonated triplet ketene species is bent as expected, and two isomers of this ion that differ in energy by 23 kJ mol⁻¹ and result from different orientations of the hydrogen atoms on oxygen and the vicinal carbon atom lie ~25 kJ mol⁻¹ below complex 1. Hydrogen atom migration in protonated ketene from the geminal carbon to oxygen generates a species of nominal structure $[\text{H}_2\text{O}-\text{CCH}]^+$, denoted 4 in Fig. 5. The barrier for this hydrogen atom migration is almost twice as large (~375 kJ mol⁻¹) as that for the shift between two carbon atoms. Intermediate 4 lies ~230 kJ mol⁻¹ above complex 1. Complex 4 may dissociate to $\text{CCH}^+ + \text{H}_2\text{O}$, the products of a nominal hydride transfer reaction.

The hydrogen atom bound to the oxygen atom in protonated ketene may undergo a 1,2-shift over a barrier of ~130 kJ mol⁻¹ to form the vinyloxy cation 5, lying ~20 kJ mol⁻¹ below protonated ketene. The bond order of the C–O bond is 1.92, confirming that this species is the keto isomer of the $[\text{C}_2\text{H}_3\text{O}]^+$ system. Carbon-carbon bond cleavage in structure 5 is expected to lead to $^3\text{CH}_2$ and HCO^+ . A second 1,2-migration of this hydrogen atom to the vicinal carbon results in the acetyl cation, CH_3CO^+ , denoted 6. The barrier for this hydrogen atom migration is ~234 kJ mol⁻¹.

The DFT calculations indicate pathways for the formation of the reaction products ${}^3\text{CH}_2+\text{HCO}^+$ (exothermic by $\sim 309\text{ kJ mol}^{-1}$) and $\text{C}_2\text{H}^++\text{H}_2\text{O}$ (exothermic by $\sim 200\text{ kJ mol}^{-1}$). The fact that these products were not observed requires a consideration of the rates of formation of intermediate 1 and the isomerization rates to form complexes 3, 4, and 5, which are precursors to these products. The isomerization rates were estimated with Rice-Ramsperger-Kassel-Marcus (RRKM) statistical calculations^{19–22} performed with the vibrational frequencies of the relevant complexes and transition states obtained from DFT calculations. All the rate constants reported here refer to the intermediate collision energy. The calculations show that complex 2 isomerizes to 1 with a rate of $2 \times 10^{13}\text{ s}^{-1}$. The isomerization rate for the 1,2-hydrogen atom migration converting the enol complex 1 to protonated ketene, 3, is $1 \times 10^{12}\text{ s}^{-1}$. The rate of the hydrogen atom migration converting protonated ketene to the keto isomer of $[\text{C}_2\text{H}_3\text{O}]^+$, complex 5, is comparable, approximately $2 \times 10^{12}\text{ s}^{-1}$. The highest barrier for isomerization, in which hydrogen migrates from carbon to oxygen to yield complex 4, results in a rate of $4 \times 10^{10}\text{ s}^{-1}$.

All of the isomerization rates of complexes arising from the initially formed enol diradical cation, complex 1, are comparable to or less than the rotational frequencies of the corresponding intermediate complexes, suggesting that if a significant fraction of collisions branched to complex 1, significant fluxes of C_2H^+ and HCO^+ products would be observed. Moreover, one would expect the product flux distributions to show broad angular distributions consistent with complexes that decay on a time scale comparable to a rotational period. The absence of such products suggests that the low impact parameter collisions required to form complex 1 occur with low probability. The proton transfer and charge transfer products are clearly formed in large impact parameter collisions, suggesting that the centrifugal barrier associated with the long-range attractive potential of the approaching reactants prevents the reactants from reaching the short range part of the potential where C–O bond formation occurs. In previous works,^{4,5,23–25} we have shown that the electrostatic complexes that characterize reactions proceeding through large impact parameters decay with rates near 10^{14} s^{-1} , further suggesting that processes that may occur via slow isomerization pathways will result in product levels below the detection limit.

VI. DISCUSSION

The charge transfer process appears to proceed as a direct reaction with a long-range electron jump. It has been established in many cases that electron-transfer reactions in ion-molecule collisions at thermal energies are governed by energy resonance and Franck-Condon effects.^{26,27} In the present system, the recombination energy of OH^+ is 13.02 eV.²⁸ There is no matching band at this energy in the photoelectron spectrum of C_2H_2 . The closest ionic state is the $1\ ^2\Pi_u$ state at 11.40 eV.²⁹ Therefore neither energy resonance nor favorable Franck-Condon factors, the two criteria for efficient reactions, are met. As discussed by Mayhew,³⁰ distortion of the molecular potential surface by the electric

field of the reacting ion, leading to a significant change in the Franck-Condon factors prior to charge transfer, may account for the observation of fast charge transfer reactions, in which the recombination energy of the ion falls outside the Franck-Condon envelope of a photoelectron band. This seems to be true for reactions involving polyatomic species with large polarizability. C_2H_2 has a polarizability of $3.23 \times 10^{-24}\text{ cm}^3$,³⁰ large enough to invoke such a distortion picture. Listed in Table I, the translational exothermicity Q is defined as the difference of the relative energy between the products and reactants. At all three collision energies, the Q values are very close to zero, which, in conjunction with the angular distributions, indicates that there is almost no momentum transfer after charge transfer. It is consistent with our experimental results, implying large impact parameter collisions.

The proton transfer process forming C_2H_3^+ exhibits many characteristics of direct proton transfer that we have studied recently in this laboratory.^{3–5,23–25,31} This proton transfer reaction is another example of a heavy+light-heavy (H+LH) system in which a light particle, H, is transferred between heavier molecular fragments. The potential energy surface for this transfer, expressed in scaled and skewed coordinates,³² is characterized by a very acute angle, 18° , between the entrance and exit channels. If the collision energy is low, the reaction trajectory does not have enough energy to penetrate into the narrow corner of such highly skewed surfaces; rather, it will rather cut the corner separating the entrance and exit valleys with a strong propensity. These motions correspond to light atom transfer from a configuration in which both the cleaving and incipient bonds are extended from equilibrium bond lengths with little momentum transfer to the departing heavy atoms, yielding reaction products that are vibrationally excited. This mechanism is described as “mixed energy release.”^{33–36} The data at the lowest collision energy show that 76% of the available energy is partitioned in product internal excitation. 93% of the reaction exothermicity is transformed into internal excitation, consistent with an early release of the exothermicity with the nascent bond extended from its equilibrium configuration, as expected for mixed energy release.

More detailed insight into the reactive dynamics comes from the experimental data at higher collision energies. The concept of “induced repulsive energy release” was introduced to address partitioning of incremental translational energy on H+LH potential surfaces.³⁷ In this picture, reactive trajectories with excess translation penetrate far into the corner of the highly skewed potential surface where both the forming and breaking bonds are compressed. The trajectory moves into the exit valley with little motion perpendicular to the reaction coordinate, yielding products with high translational excitation. At the intermediate collision energy of 0.71 eV, 69% of the incremental translational energy appears in product translation; at the highest collision energy of 1.18 eV, a significantly increased fraction, 91% of the increment, partitions in product translation. The corner cutting trajectories that produce vibrationally excited products at lower collision energies are replaced by trajectories at higher translational energy that are more effective at reaching the

compressed configurations that facilitate translation in the separating products. This proton transfer reaction provides an excellent example of induced repulsive energy release.

VII. CONCLUSIONS

The crossed beam technique and DFT calculations are used to study the reaction dynamics between OH^+ and C_2H_2 . The c.m. flux distributions of both charge transfer and proton transfer product ions at three energies exhibit sharp asymmetry, with the maxima close to the velocity and direction of the precursor acetylene beam. The results indicate that both reactions proceed through direct collisions with large impact parameters. Despite the lack of energy resonance and favorable Franck-Condon factors, a distortion in the Franck-Condon envelope of the neutral molecule may contribute to the efficiency of the charge transfer reaction. The proton transfer shows characteristics of both mixed energy release and induced repulsive energy release typical of the energy dependence of the dynamics associated with the $\text{H}+\text{LH}$ mass combination.

We hope that the study of this simple system will provide a foundation for detailed dynamical calculations to confirm and extend the present conclusions and for studies on more complex systems.

¹R. Cvetanovic, *Adv. Photochem.* **1**, 115 (1963).

²X. Cai, Y. Li, and J. M. Farrar, *Int. J. Mass. Spectrom.* **241**, 271 (2005).

³L. Liu, X. Cai, Y. Li, E. R. O'Grady, and J. M. Farrar, *J. Chem. Phys.* **121**, 3495 (2004).

⁴L. Liu, Y. Li, and J. M. Farrar, *J. Chem. Phys.* **123**, 094304 (2005).

⁵L. Liu, Y. Li, and J. M. Farrar, *J. Chem. Phys.* **124**, 124317 (2006).

⁶A. M. Schmoltner, P. M. Chu, and Y. T. Lee, *J. Chem. Phys.* **91**, 5365 (1989).

⁷D. F. Varley, D. J. Levandier, and J. M. Farrar, *J. Chem. Phys.* **96**, 8806 (1992).

⁸P. E. Siska, *J. Chem. Phys.* **59**, 6052 (1973).

⁹Z. Herman, *Int. J. Mass. Spectrom.* **212**, 413 (2001).

¹⁰A. M. Schmoltner, P. M. Chu, R. J. Brudzynski, and Y. T. Lee, *J. Chem.*

Phys. **91**, 6926 (1989).

¹¹A. R. Clemo, G. L. Duncan, and R. Grice, *J. Chem. Soc., Faraday Trans. 2* **78**, 1231 (1982).

¹²G. Capozza, E. Segoloni, F. Leonori, G. G. Volpi, and P. Casavecchia, *J. Chem. Phys.* **120**, 4557 (2004).

¹³L. Salem and C. Rowland, *Angew. Chem., Int. Ed. Engl.* **11**, 92 (1972).

¹⁴K. Yamaguchi, S. Yabushita, T. Fueno, S. Kato, and K. Morokuma, *Chem. Phys. Lett.* **80**, 27 (1980).

¹⁵L. B. Harding and A. F. Wagner, *J. Phys. Chem.* **90**, 2974 (1986).

¹⁶M. J. Frisch, G. W. Trucks, H. B. Schlegel *et al.*, GAUSSIAN 98, A.11.1 ed., Gaussian, Inc., Pittsburgh, PA, 2001.

¹⁷See EPAPS Document No. E-JCPSA6-125-115637 for structural parameters, vibrational frequencies, and electronic energies of all intermediates and transition states. This document can be reached via a direct link in the online article's HTML reference section or via the EPAPS homepage (<http://www.aip.org/pubservs/epaps.html>).

¹⁸T. J. Lee and H. F. Schaefer III, *J. Chem. Phys.* **85**, 3437 (1986).

¹⁹O. K. Rice and H. C. Ramsperger, *J. Am. Chem. Soc.* **49**, 1617 (1927).

²⁰L. S. Kassel, *J. Phys. Chem.* **32**, 225 (1928).

²¹R. A. Marcus and O. K. Rice, *J. Phys. Colloid Chem.* **55**, 894 (1951).

²²T. Baer and W. L. Hase, *Unimolecular Reaction Dynamics: Theory and Experiments* (Oxford University Press, New York, 1996).

²³Y. Li and J. M. Farrar, *J. Chem. Phys.* **120**, 199 (2004).

²⁴Y. Li and J. M. Farrar, *J. Phys. Chem. A* **108**, 9876 (2004).

²⁵Y. Li, L. Liu, and J. M. Farrar, *J. Phys. Chem. A* **109**, 6392 (2005).

²⁶M. T. Bowers and D. D. Elleman, *Chem. Phys. Lett.* **16**, 486 (1972).

²⁷J. B. Laudenslager, W. T. Huntress, and M. T. Bowers, *J. Chem. Phys.* **61**, 4600 (1974).

²⁸NIST, <http://webbook.nist.gov/chemistry/>

²⁹K. Kimura, S. Katsumata, Y. Achiba, T. Yamazaki, and S. Iwata, *Handbook of HeI Photoelectron Spectra of Fundamental Organic Molecules* (Halsted, New York, 1980).

³⁰C. A. Mayhew, *J. Phys. B* **25**, 1865 (1992).

³¹W. K. Li, S. W. Chiu, Z. X. Ma, C. L. Liao, and C. Y. Ng, *J. Chem. Phys.* **99**, 8440 (1993).

³²J. O. Hirschfelder, *Int. J. Quantum Chem., Symp.* **3**, 17 (1969).

³³K. G. Anlauf, P. J. Kuntz, D. H. Maylotte, P. D. Pacey, and J. C. Polanyi, *Discuss. Faraday Soc.* **44**, 183 (1967).

³⁴K. G. Anlauf, J. C. Polanyi, W. H. Wong, and K. B. Woodall, *J. Chem. Phys.* **49**, 5189 (1968).

³⁵D. H. Maylotte, J. C. Polanyi, and K. B. Woodall, *J. Chem. Phys.* **57**, 1547 (1972).

³⁶C. A. Parr, J. C. Polanyi, and W. H. Wong, *J. Chem. Phys.* **58**, 5 (1973).

³⁷A. M. G. Ding, L. J. Kirsch, D. S. Perry, J. C. Polanyi, and J. L. Schreiber, *Faraday Discuss. Chem. Soc.* **55**, 252 (1973).